Deformed band structures at high spin in ^{200}Tl

Soumik Bhattacharya,[1,2] S. Bhattacharyya,[1,2,*] S. Das Gupta,[1,†] H. Pai,[1] G. Mukherjee,[1,2] R. Palit,[3] F. R. Xu,[4] Q. Wu,[4] A. Shrivastava,[5] Md. A. Asgar,[1,2] R. Banik,[1,2] T. Bhattacharjee,[1,2] S. Chanda,[6] A. Chatterjee,[5] A. Goswami,[7] V. Nanal,[3] S. K. Pandit,[5] S. Saha,[3] J. Sethi,[3] T. Roy,[1,2] and S. Thakur[3]

[1]*Variable Energy Cyclotron Centre, 1/AF Bidhannagar, Kolkata 700064, India*

[2]*Homi Bhabha National Institute, Training School Complex, Anushaktinagar, Mumbai 400094, India*

[3]*Department of Nuclear and Atomic Physics, Tata Institute of Fundamental Research, Mumbai 400005, India*

[4]*State Key Laboratory of Nuclear Physics and Technology, School of Physics, Peking University, Beijing 100871, Peoples Republic of China*

[5]*Nuclear Physics Division, Bhabha Atomic Research Centre, Mumbai 400085, India*

[6]*Fakir Chand College, Diamond Harbour, West Bengal, India*

[7]*Saha Institute of Nuclear Physics, Kolkata 700064, India*

(Received 5 July 2016; revised manuscript received 9 September 2016; published 3 January 2017)

High-spin band structures of ^{200}Tl have been studied by γ-ray spectroscopic methods using the ^{198}Pt(^{7}Li ,5n)^{200}Tl reaction at 45 MeV of beam energy. The level scheme of ^{200}Tl has been extended significantly and several new band structures have been established with the observation of 60 new transitions. The $\pi h_{9/2} \otimes \nu i_{13/2}$ oblate band has been extended beyond the particle alignment frequencies. The band structures and the other excited states have been compared with the neighboring odd-odd Tl isotopes. Total Routhian surface calculations have been performed to study the deformation and shape changes as a function of spin in this nucleus. These calculations could reproduce the particle alignment frequency and suggest that the neutron pair alignment in $\nu i_{13/2}$ orbital induces γ softness in ^{200}Tl.

DOI: 10.1103/PhysRevC.95.014301

I. INTRODUCTION

Investigations of odd-proton and odd-neutron nuclei near a doubly magic shell closure have proven to be invaluable in understanding the evolution of active orbitals, responsible for the nuclear shapes and structure of excited states in nearby nuclei. The odd-odd nuclei on the other hand are known to provide access to valuable inputs for the proton-neutron residual interaction. The nuclei around doubly magic ^{208}Pb ($Z = 82$ and $N = 126$) are of special interest in this regard to understand the various types of particle-core coupling and collective excitations [1,2]. In particular, intrinsic states based on intruder orbitals play an important role to study the deformation-driving effects near a shell closure [3]. The interplay of single-particle and collective excitations near a shell closure can be probed by investigation of high-spin states of nuclei with few valence nucleons outside the even-even core. Study of the high-spin states in thallium (Tl) isotopes, with only one proton hole and an odd number of neutron holes with respect to the ^{208}Pb core can provide important information in understanding the interaction of valence particles with the underlying core around $Z = 82$, as a function of angular momentum.

Spectroscopy of odd-odd Tl isotopes is the subject of many recent experimental investigations. The chain of odd-odd Tl isotopes exhibits a variety of shapes and structures, ranging from simple low-spin single-particle excitations in ^{202,206}Tl [4,5], to complex configurations involving core excitations in neutron rich ^{204}Tl [6], oblate deformed band structures based on intruder configuration in $^{190-200}$Tl isotopes [7–12], the recent observation of a magnetic rotational band in ^{194}Tl [9], as well as chiral band structures associated with the triaxial deformation reported in ^{194,198}Tl [13,14]. For odd-odd Tl isotopes the ground-state spin is 2^- corresponding to the occupation of the $\pi s_{1/2}$ orbital below the $Z = 82$ spherical core and the $\nu p_{3/2}$ orbital below $N = 126$. The intruder $\pi h_{9/2}$ orbital above the $Z = 82$ shell closure is accessible by the odd proton in case of oblate deformation. A remarkable systematics of collective oblate yrast structures based on high-j proton intruder orbital $\pi h_{9/2}$ and neutron orbital $\nu i_{13/2}$ have been observed over a large isotopic chain of Tl nuclei, ranging from neutron deficient ^{190}Tl ($N = 109$) [7] near the midshell to ^{200}Tl ($N = 119$) [12] near the shell closure. These deformed band structures can be understood to be due to the presence of collective bands based on high-j orbitals $\pi h_{9/2}$ and $\nu i_{13/2}$ in neighboring odd-A Tl and Hg nuclei, respectively. But in most of the cases, high-spin states beyond the first band crossing are not investigated in detail, except in a few cases, such as, ^{194}Tl [9,13] and ^{198}Tl [14]. The $\pi h_{9/2} \otimes \nu i_{13/2}$ oblate band structure could not be observed in heavier Tl isotopes beyond ^{200}Tl, where only a few members of this band are known [12]. As one moves towards $N = 126$ shell closure, the heavier Tl isotopes are expected to have spherical structure and coupled states of ^{208}Pb core with the valence particles are observed. Thus ^{200}Tl is situated on the boundary of collective oblate deformation resulting from deformed Hg core and spherical shape dominated by single-particle excitations with respect to the ^{208}Pb core. In addition, the recent observations of chiral partner bands in ^{194}Tl [13] and ^{198}Tl [14] have generated further interest in high-spin structure of the next odd-odd isotope ^{200}Tl.

Information on the low-spin states in ^{200}Tl come from the electron-capture-decay study of ^{200}Pb [15]. Prior to the present

*sarmi@vecc.gov.in

†Present Address: Heritage Institute of Technology, Anandapur, Kolkata 700107, India.

work, the only high-spin γ-ray spectroscopic information on ^{200}Tl was known from ^{6}Li-induced fusion evaporation reaction [12], measured by using two Ge(Li) detectors. With the availability of the new generation of high-resolution, high-efficiency detector arrays, more complete information about the detail band structure of ^{200}Tl has become possible to obtain. The present work reports the high-spin structure of ^{200}Tl beyond band crossing of yrast oblate structure and observation of other near-yrast band structures.

II. EXPERIMENT

The high-spin states in ^{200}Tl have been populated by the fusion-evaporation reaction ^{198}Pt(^{7}Li ,5n) at the beam energy of 45 MeV, obtained from the BARC-TIFR Pelletron LINAC facility in Mumbai, India. The target used was a 1.3-mg/cm^2-thick ^{198}Pt self-supporting foil with 95.7% enrichment. Other than the dominant fusion evaporation channels resulting in ^{200,201}Tl, significant contributions of ^{198,199}Au and ^{199,200}Hg residues resulting from α and t capture of a ^{7}Li beam, having $(\alpha + t)$ cluster structure, were observed in the present experiment. The measurements were carried out with the Indian National Gamma Array (INGA), configured with 15 Compton-suppressed clover high-purity Ge (HPGe) detectors for the present experiment, to detect γ rays in coincidence. A limited set of data was also taken in singles mode. The detectors were arranged in six different angles with two detectors each at 40°, 65°, 115°, 140°, while four detectors were at 90° and three were at 157°. The time-stamped data were collected by using a PCI-PXI-based digital data-acquisition system developed by XIA-LLC with a sampling rate of 100 MHz. Six Pixie-16 modules were used to process preamplifier pulses from clover HPGe detectors and each channel was processed after satisfying the veto condition of respective bismuth-germanate (BGO) anti-Compton shield. Further details of this data-acquisition system can be found in Ref. [16]. The energy and efficiency calibrations of each detector were done with ^{133}Ba and ^{152}Eu standard sources placed at the target position.

III. DATA ANALYSIS

The raw data were sorted by using the Multi pARameter time-stamped based COincidence Search (MARCOS) [16] sorting program, developed at the TIFR, Mumbai, to generate the symmetric E_γ-E_γ matrix and E_γ-E_γ-E_γ cube, after gain matching the energy of each clover detector to 0.5 keV/channel and 2 keV/channel, respectively. A coincidence time window of 400 ns was selected to generate the above matrix and the cube. The analysis of E_γ-E_γ matrices and the γ-γ-γ cube were carried out by using RADWARE [17] and INGASORT [18] analysis packages to obtain the coincidence relationships among various transitions, which were used further to construct the level scheme.

A representative coincidence spectrum corresponding to γ rays detected in coincidence with the 119, 217, 230, or 348 keV gamma transitions of the yrast band in ^{200}Tl, obtained from the E_γ-E_γ matrix, is shown in Fig. 1. Most of the new transitions can be identified from this coincidence spectrum. A total of 60 new transitions in ^{200}Tl have been assigned from

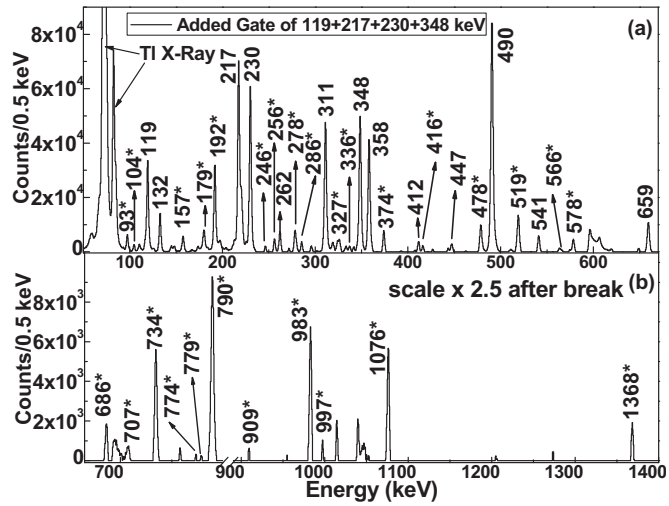

FIG. 1. Spectrum of γ rays detected in coincidence with the 119, 217, 230, or 348 keV γ transitions. (a) The lower-energy part and (b) the higher-energy part of the spectrum. The new peaks observed in the present work are marked as "*."

the present work. As the γ-ray energies are very similar of those in the residues arising from different incomplete fusion channels, the coincidence relationships were mainly obtained from the double-gated spectra generated from the E_γ-E_γ-E_γ cube. In this analysis procedure, the information on yields of complete and incomplete fusion, the capture of various cluster fragments, and the particle-gated gamma spectra obtained from the same reaction previously [19] have also been utilized for the assignment of γ rays in ^{200}Tl.

The information on the multipolarities of the γ rays were primarily obtained from the analysis of the ratio of directional correlation from oriented states (DCO) [20], for which an asymmetric γ-γ matrix, with the X axis containing the data from the 157° (θ_1) detectors and the Y axis containing the data from the 90° (θ_2) detectors was generated. The DCO ratio of a transition γ_1 is then obtained from the ratio of its intensities at two angles θ_1 and θ_2, gated by another transition γ_2 of known multipolarity, as per the following expression:

$$R_{\rm DCO} = \frac{I_{\gamma_1} \text{ at } \theta_1, \text{ gated by } \gamma_2 \text{ at } \theta_2}{I_{\gamma_1} \text{ at } \theta_2, \text{ gated by } \gamma_2 \text{ at } \theta_1}. \quad (1)$$

For a pure stretched quadrupole or dipole transition, the R_{DCO} should be close to unity when gated by a transition of same multipolarity. For the gating transition of different multipolarity, the R_{DCO} value depends on the nature of the gating transition. In the present analysis, the typical values of R_{DCO} come out to be ~1.0 (2.0) for pure stretched dipole (quadrupole) transitions when gated with a stretched pure dipole transition. In the present experiment, for a stretched quadrupole gate, the values are found to be ~0.5 (1.0) for pure stretched dipole (quadrupole) transitions. These values are corroborated by the analysis R_{DCO} values of known $E2$ and $M1$ transitions of neighboring Tl, Hg, and Au nuclei, populated in the same reaction. For example, in the case of ^{201}Tl, populated in the same experiment, the DCO ratios of the 423 keV ($E2$) and 120 keV ($M1$) transitions come

TABLE I. The energies E_γ and relative intensities I_γ of the γ rays placed in ^{200}Tl along with the spin and parity of the initial J_i^π and final J_f^π states and the energy of the initial state (E_i). The measured values of $R_{\rm DCO}$ and $\Delta_{\rm IPDCO}$ are also shown along with the proposed multipolarities of the γ rays.

E_γ (keV)	E_i (keV)	$J_i^\pi \rightarrow J_f^\pi$	I_γ (Err)[a]	$R_{\rm DCO}$ (Err)	$\Delta_{\rm IPDCO}$ (Err)	Deduced multipolarity
(3.4)[b]	1247.4	$(8^-) \rightarrow (9^-)$				$(M1+E2)$
(16.5)[b]	1892.5	$(11^+) \rightarrow (10^+)$				$(M1+E2)$
(56.7)[b]	3856.8	$18^- \rightarrow (17^-)$				$(M1+E2)$
(56.3)[b]	3313.4	$14^+ \rightarrow 13^+$				$(M1)$
76.1(1)	1323.0	$9^- \rightarrow 8^-$				$(M1+E2)$
93.1(3)	3313.4	$14^+ \rightarrow 15^+$	2.04(51)			$(M1)$
104.4(2)	4032.6	$18^+ \rightarrow 17^+$	2.19(9)	0.99(18)[c]		$M1+E2$
119.2(1)	1442.1	$10^- \rightarrow 9^-$	19.36(96)	1.11(3)[c]		$M1$
132.4(1)	886.0	$8^+ \rightarrow 7^+$	10.79(54)	1.30(3)[c]		$M1+E2$
157.3(1)	3928.2	$17^+ \rightarrow 16^+$	4.53(17)	0.91(14)[c]		$M1$
175.7(1)	1892.5	$(11^+) \rightarrow (10^+)$	10.56(45)	0.75(12)[d]		$(M1+E2)$
179.2(1)	2071.7	$12^- \rightarrow (11^+)$	11.92(48)	0.82(8)[d]		$(E1)$
179.8(1)	3770.9	$16^+ \rightarrow 15^+$	2.88(14)	1.08(7)[c]		$M1+E2$
191.0(1)	3799.5	$(17^-) \rightarrow 16^-$		0.55(4)[e]		$(M1)$
192.0(2)	3856.8	$18^- \rightarrow 17^-$	3.40(19)			$(M1+E2)$
192.0(1)	4048.8	$19^{(-)} \rightarrow 18^-$	12.62(66)	0.58(1)[f]		$(M1+E2)$
194.7(1)	1442.1	$10^- \rightarrow 8^-$	2.06(33)			$(E2)$
196.0(1)	2634.0	$(-) \rightarrow (12^+)$	1.58(22)			
211.0(2)	5038.7	$(-) \rightarrow (21^-)$	0.70(15)			$(M1+E2)$
213.0(2)	754.0	$7^+ \rightarrow 4^-$				$E3$[g]
217.0(2)	541.0	$4^- \rightarrow 3^-$				$M1$[g]
217.2(1)	1659.3	$11^- \rightarrow 10^-$	66(3)	0.42(3)[h]	−0.06(3)	$M1+E2$
220.4(1)	1244.0	$9^- \rightarrow 7^-$		0.84(17)[h]	0.35(2)	$E2$
221.0(1)	762.0	$6^+ \rightarrow 4^-$				$(M2)$
229.8(1)	1889.1	$12^- \rightarrow 11^-$	51(2)	0.46(1)[h]	−0.04(2)	$M1+E2$
246.2(1)	4898.3	$(21^+) \rightarrow (20^+)$	3.57(12)	1.08(22)[c]	−0.32(14)	$(M1+E2)$
256.0(1)	3282.1	$16^- \rightarrow 15^-$	3.34(25)	0.47(7)[h]	−0.15(8)	$M1$
261.7(1)	4032.6	$18^+ \rightarrow 16^+$	1.53(13)		0.06(9)	$(E2)$
261.6(1)	1023.6	$7^- \rightarrow 6^+$		0.49(7)[h]	0.12(9)	$E1$
271.2(3)	4320.0	$20^{(-)} \rightarrow 19^{(-)}$	0.93(3)	0.33(4)[f]		$(M1+E2)$
278.0(1)	3591.4	$15^+ \rightarrow 14^+$	7.48(25)	0.76(5)[c]	−0.07(5)	$M1+E2$
278.0(1)	4652.1	$(20^+) \rightarrow 19^+$	1.12(17)			$(M1+E2)$
285.5(1)	5183.3	$(22^+) \rightarrow (21^+)$	1.80(11)		−0.08(15)	$(M1+E2)$
285.7(1)	5041.5	$22^{(-)} \rightarrow 21^{(-)}$	0.99(19)	0.40(5)[f]	−0.06(2)	$M1+E2$
287.7(1)	1173.7	$8^+ \rightarrow 8^+$	56(1)	1.33(5)[d]	0.13(7)	$M1+E2$
310.7(1)	2548.1	$14^- \rightarrow 13^-$	31(2)	0.47(2)[e]	−0.05(2)	$M1$
311.7(1)	3337.8	$16^- \rightarrow 15^-$	3.78(32)	0.39(4)[h]		$(M1+E2)$
324.0(3)	324.0	$3^- \rightarrow 2^-$				$M1$[g]
326.0(2)	1349.6	$(8^-) \rightarrow 7^-$				$(M1+E2)$
326.4(1)	3608.4	$16^- \rightarrow 16^-$	1.61(16)	0.58(4)[e]	−0.02(9)	$M1+E2$
327.0(2)	3664.8	$(17^-) \rightarrow 16^-$	0.34(7)			$(M1+E2)$
336.3(3)	1659.3	$11^- \rightarrow 9^-$	2.51(33)	0.89(13)[h]		$E2$
337.0(4)	3928.2	$17^+ \rightarrow 15^+$				$(E2)$
341.5(1)	4374.1	$19^+ \rightarrow 18^+$	9.40(14)	0.77(13)[c]	−0.15(17)	$M1$
348.3(1)	2237.4	$13^- \rightarrow 12^-$	50(1)	0.72(1)[c]	−0.04(2)	$M1+E2$
358.1(1)	1244.0	$9^- \rightarrow 8^+$	36.83(67)	0.60(2)[h]	0.09(3)	$E1$
373.9(1)	2922.0	$15^- \rightarrow 14^-$	7.48(38)	0.44(4)[h]	−0.04(4)	$M1+E2$
384.0(1)	1733.6	$(9^-) \rightarrow (8^-)$				$(M1+E2)$
412.4(1)	2071.7	$12^- \rightarrow 11^-$	10.12(53)	0.84(20)[c]	−0.10(4)	$M1$
415.8(1)	3337.8	$16^- \rightarrow 15^-$	4.93(35)	0.48(4)[f]	−0.11(7)	$M1$
420.0(1)	1173.7	$8^+ \rightarrow 7^+$	23.21(61)		0.02(3)	$M1+E2$
435.8(1)	4755.8	$21^{(-)} \rightarrow 20^{(-)}$				$(M1)$
447.0(2)	1889.1	$12^- \rightarrow 10^-$	10.49(51)	1.07(8)[h]	0.05(4)	$E2$
457.3(8)	3770.9	$16^+ \rightarrow 14^+$	1.95(9)			$(E2)$

TABLE I. (*Continued.*)

E_γ (keV)	E_i (keV)	$J_i^\pi \rightarrow J_f^\pi$	I_γ (Err)[a]	R_{DCO} (Err)	Δ_{IPDCO} (Err)	Deduced multipolarity
478.0(1)	3026.1	$15^- \rightarrow 14^-$	6.74(49)	0.30(2)[h]	−0.03(3)	$M1+E2$
490.4(1)	1244.0	$9^- \rightarrow 7^+$	100(4)	1.01(2)[h]	−0.10(2)	$M2$
492.4(1)	3337.8	$16^- \rightarrow (14^-)$	2.34(18)	0.86(14)[f]		$(E2)$
493.8(7)	1247.4	$8^- \rightarrow 7^+$	5.89(69)			$(E1)$
517.4(1)	3799.5	$17^- \rightarrow 16^-$	2.64(14)	0.39(8)[e]	−0.18(7)	$M1+E2$
519.1(1)	3856.8	$18^- \rightarrow 16^-$	13.86(58)	0.82(4)[i]	0.14(4)	$E2$
541.0(4)	541.0	$4^- \rightarrow 2^-$				$E2$[g]
543.1(1)	1716.7	$(10^+) \rightarrow 8^+$	19.77(45)	1.29(19)[d]	0.06(4)	$(E2)$
562.0(3)	2438.0	$(12^+) \rightarrow (10^+)$	5.73(17)	1.20(17)[d]		$(E2)$
565.9(3)	3114.0	$(-) \rightarrow 14^-$	3.59(43)			
574.7(2)	3856.8	$18^- \rightarrow 16^-$	1.36(38)	0.70(11)[e]		$(E2)$
578.3(2)	2237.4	$13^- \rightarrow 11^-$	13.43(63)	1.87(15)[c]	0.14(5)	$E2$
619.5(3)	4652.1	$(20^-) \rightarrow 18^-$	1.98(9)		0.12(2)	$(E2)$
659.0(1)	2548.1	$14^- \rightarrow 12^-$	20.42(78)	1.02(9)[i]	0.14(4)	$E2$
686.4(1)	3608.4	$16^- \rightarrow 15^-$	2.93(30)	0.73(11)[h]	−0.10(5)	$M1+E2$
702.2(2)	1876.0	$(10^+) \rightarrow 8^+$	15.24(78)	0.92(11)[d]	0.11(5)	$(E2)$
707.2(3)	4755.8	$21^{(-)} \rightarrow 19^{(-)}$	1.57(51)	1.44(25)[f]	0.05(11)	$E2$
734.4(2)	3282.1	$16^- \rightarrow 14^-$	10.18(53)	0.85(5)[h]	0.08(4)	$E2$
742.0(2)	2813.7	$(-) \rightarrow 12^-$	2.80(89)			$(E2)$
773.4(2)	3799.5	$(17^-) \rightarrow 15^-$	1.13(17)		0.07(3)	$(E2)$
773.8(2)	2845.4	$(14^-) \rightarrow 12^-$	1.07(9)	1.60(55)[f]		$(E2)$
778.8(2)	4827.6	$21^{(-)} \rightarrow 19^{(-)}$	2.19(22)	1.35(28)[f]		$(E2)$
789.7(1)	3337.8	$16^- \rightarrow 14^-$	16.88(72)	0.85(6)[h]	0.15(4)	$E2$
909.4(2)	4958.2	$21^{(-)} \rightarrow 19^{(-)}$	1.85(20)	0.85(7)[f]		$(E2)$
971.0(2)	2630.3	$(12^-) \rightarrow 11^-$	1.85(17)		−0.21(10)	$(M1)$
982.9(2)	3220.3	$15^+ \rightarrow 13^-$	5.82(36)	1.82(19)[c]	−0.17(4)	$M2$
997.3(2)	2886.4	$(14^+) \rightarrow 12^-$	2.42(20)	1.78(59)[c]	−0.14(11)	$(M2)$
1076.2(2)	3313.4	$14^+ \rightarrow 13^-$	6.97(40)	0.95(10)[c]	0.05(4)	$E1$
1368.1(2)	3257.1	$13^+ \rightarrow 12^-$	4.23(28)	1.03(13)[c]	0.06(5)	$E1$

[a]Relative γ-ray intensities are estimated from prompt spectra and normalized to 100 for the total intensity of the 490.4 keV γ ray.
[b]Unobserved transitions.
[c]From the 358.1 keV ($E1$) DCO gate.
[d]From the 132.4 keV ($M1+E2$) DCO gate.
[e]From the 734.4 keV ($E2$) DCO gate.
[f]From the 519.1 keV ($E2$) DCO gate.
[g]Adopted from Ref. [12].
[h]From the 659.0 keV ($E2$) DCO gate.
[i]From the 789.7.0 keV ($E2$) DCO gate.

out as 1.92(4) and 1.04(14), respectively when gated by the known dipole transition of 785 keV. From the 652 keV quadrupole ($E2$) gate, the DCO ratio of the 1142 keV ($E1$) γ transition comes out as 0.46(4), whereas for the 443 keV ($E2$) transition the value of R_{DCO} is 0.99(4). In ^{200}Hg, for the another quadrupole ($E2$) gate of the 579 keV transition, the R_{DCO} value for the 759 keV quadrupole ($E2$) transition has been obtained as 0.95(2), whereas the 904 keV dipole ($E1$) transition it comes out to be of 0.54(3). The multipolarity of various transitions in ^{200}Tl are obtained from the deduced DCO ratios, either from the known quadrupole gate of 659 keV ($E2$) and dipole gate of 358 keV ($E1$) or gate of the other deduced dipole or quadrupole transitions, as shown in Table I.

The parity of most of the excited states could be assigned from the polarization measurement by exploiting the configuration of the four Ge crystals in a clover detector. The information regarding the type (electric or magnetic) of the transitions are obtained from the integrated polarization directional correlation (IPDCO) asymmetry parameter following the prescription of Refs. [21,22]. The Compton-suppressed clover detectors of INGA, placed at 90° with respect to beam direction, were used for polarization measurements. The IPDCO asymmetry parameter is defined as

$$\Delta_{IPDCO} = \frac{a(E_\gamma)N_\perp - N_\parallel}{a(E_\gamma)N_\perp + N_\parallel}, \quad (2)$$

where $N_\parallel$ and $N_\perp$ are the number of counts corresponding to the Compton scattered components of a γ ray in the planes parallel and perpendicular to the reaction plane, respectively. Here, $a(E_\gamma)$ is the correction factor due to geometrical asymmetry of the detector array or asymmetry in the response of the four crystals of a clover Ge detector.

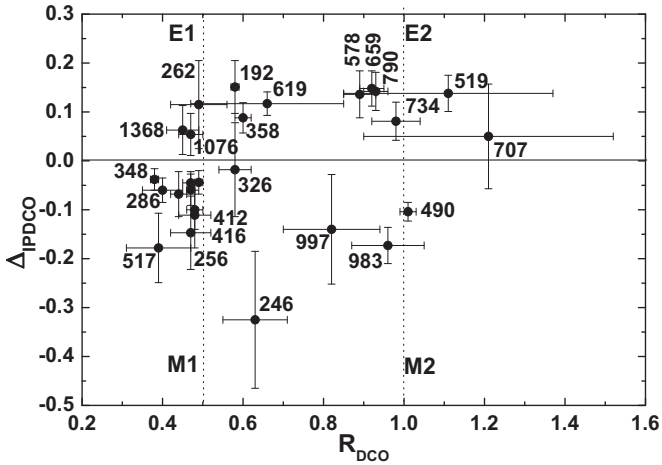

FIG. 2. DCO ratio vs polarization asymmetry of various transitions in ^{200}Tl obtained with different quadrupole gates as indicated. The dotted lines at the X axis correspond to the values for a dipole and quadrupole transitions in a pure quadrupole gate, respectively, and are shown to guide the eye. The dotted line at the Y axis is to guide the eye for +ve and −ve values of IPDCO for electric and magnetic transitions, respectively.

This factor $[a(E_\gamma) = \mathrm{N}_\parallel/\mathrm{N}_\perp]$ can be obtained by using the scattered components of γ rays from an unpolarized source, which should be close to unity. For the present setup, this correction factor was obtained as 1.037(37) from the fitting of its variation as a function of γ-ray energy using ^{133}Ba and ^{152}Eu radioactive sources [23]. To extract the parallel and perpendicular scattered component of a γ transition, two asymmetric E_γ-E_γ matrices corresponding to parallel and perpendicular scattered events of the clover detectors at 90° along one axis and the coincident γ rays from the other detectors along another axis were constructed. From the projected spectra of the above matrices, the number of counts in the perpendicular ($N_\perp$) and parallel ($N_\parallel$) scattering for a given γ ray was obtained. The positive and negative values of Δ_{IPDCO} correspond to the electric and magnetic transitions, respectively. To check the consistency of the polarization analysis, the electromagnetic nature of the known transitions in ^{201}Tl, ^{199,200}Hg, ^{198,199}Au nuclei, produced in the same reaction, were reproduced from the polarization measurements, and it was observed that the present Δ_{IPDCO} results were in well agreement with the previous results. The deduced Δ_{IPDCO} values for various transitions in ^{200}Tl are given in Table I. The DCO ratio and Δ_{IPDCO} of various known and new transitions are also shown in a separate plot in Fig. 2.

For a stretched ($\Delta I = J_i - J_f$, with J_i and J_f being the spin of the initial and final states) pure transition, a unique multipolarity and parity of the corresponding state can be assigned from the measurement of $\mathrm{R_{DCO}}$ and Δ_{IPDCO}. But, in case of nonstretched ($\Delta I < J_i - J_f$) mixed transitions, the angular distribution of individual transition along with the polarization measurement for different mixing ratio δ also need to be considered for various possible spin sequences to assign the spin-parity of the corresponding state. For this purpose, the data set taken in singles mode was analyzed to obtain

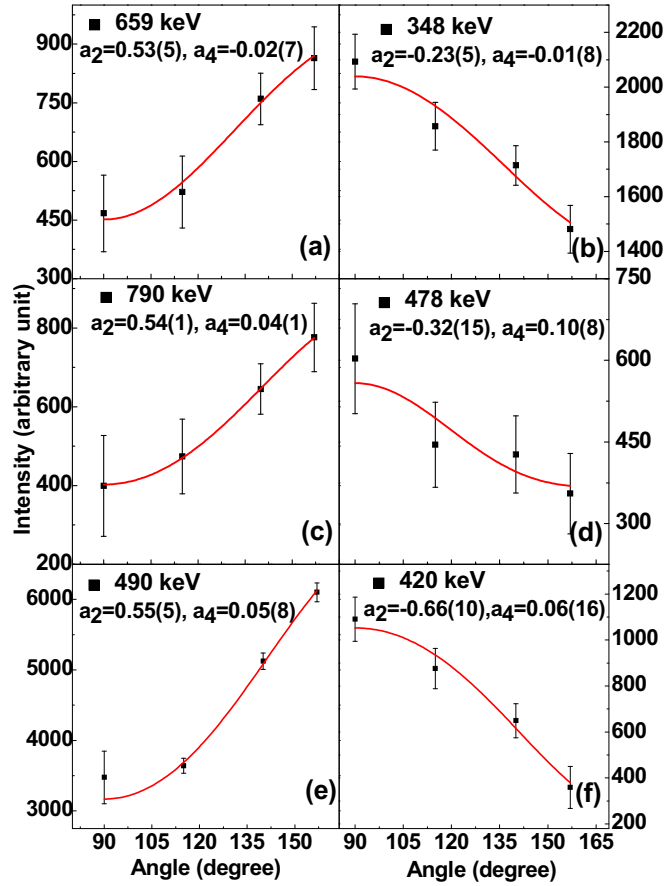

FIG. 3. Angular distribution of various transitions in ^{200}Tl obtained in the present work: (a), (c), (e) quadrupole transitions; (b), (d), (f) dipole transitions.

the angular distribution of γ rays, corrected by the detector efficiency for corresponding angle. Anisotropy parameters a_2 and a_4 corresponding to the angular distribution of the transitions are obtained by fitting the experimental angular distribution by the well-known Legendre polynomial function,

$$W(\theta) = A_0[1 + a_2 P_2(\cos\theta) + a_4 P_4(\cos\theta)], \qquad (3)$$

where θ is the detector angle with respect to the beam axis and A_0 is the normalization parameter. Angular distribution of some of the known as well as new transitions in ^{200}Tl are shown in Fig. 3. Multipolarities of various transitions have been deduced on the basis of both $\mathrm{R_{DCO}}$ values and angular distribution, wherever possible.

IV. RESULTS

The level scheme of ^{200}Tl, obtained from the present work is shown in Fig. 4. The present level scheme indicates a significant extension of the yrast band (B1) compared with earlier work [12] as well as the observation of several new band structures (B2–B4) at higher spins. The construction of the level scheme of ^{200}Tl is based on coincidence relations of identified transitions, intensity balance, $\mathrm{R_{DCO}}$, Δ_{IPDCO}, and angular-distribution measurements. A total of 60 new transitions in ^{200}Tl have been identified and placed in the

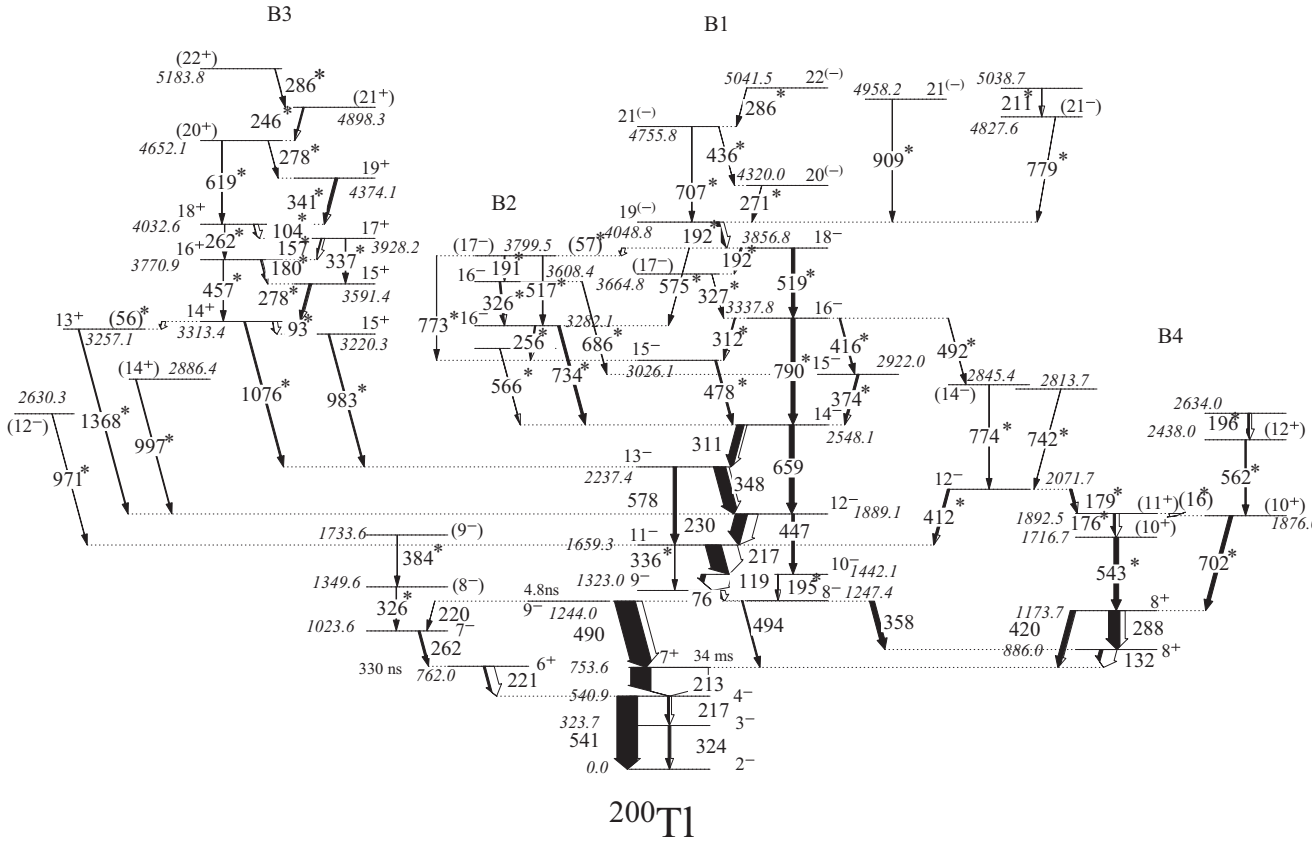

FIG. 4. Level scheme of ^{200}Tl, as obtained from the present work. New transitions are marked as "*."

level scheme, which are marked with asterisks in Fig. 4. The energies, relative intensities of the γ rays, and assigned spin-parity of various levels placed in the level scheme of ^{200}Tl from the present work are tabulated in Table I, along with other relevant quantities. The transitions up to the 2548.1 keV (14^-) level, except a few crossover $E2$ transitions, in the yrast band B1 and transitions up to 1173.7 keV level in band B4 were only known from the previous work by Kreiner *et al.* [12]. The band sequences B2 and B3 are completely new and reported for the first time from the present work. All the transitions of band B1 beyond the 2548.1 keV level and the transitions of band B4 beyond the 1173.7 keV level are also reported here for the first time. The existence of band B3 and the various connecting transitions between bands B1 and B3 can be seen from Figs. 5(a)–5(c). Figures 6(a)–6(c) represent the cascade and parallel sequences pertaining to the new transitions of band B1 reported from the present work. The extension of band B4 from the present work and the coincidence relationships among the various transitions in band B4 are represented in Figs. 7(a)–7(c).

The band B1 has been extended up to spin (22^-) with the observation of a sequence of new $M1 + E2$ transitions of 478, 312, 327, 192 (doublet), 271, and 286 keV and some of the crossover $E2$ transitions parallel to $M1$ cascades, as shown in Figs. 1 and 5(b). Placement of the 311-312 keV doublet in the level scheme (Fig. 4) could be confirmed from the double gate of 348 and 311 keV, as shown in Fig. 5(b). Individual intensities of the doublet have been obtained from their intensities in the 490 and 659 keV gates, respectively, after proper normalization. Few parallel branches have been observed beyond the 2548.1 keV (14^-) state. The 734 and 790 keV transitions are placed parallel to each other from their mutual coincidence relationships observed from $E_\gamma - E_\gamma$ matrix. The placement of 478-312 keV and 416-374 keV cascades in parallel to the 790 keV transition were established from the coincidence spectrum of 790 keV. It is also observed that the 192 keV transition is in coincidence with 517, 519, 734, and 790 keV and is present in self-coincidence as well. Moreover, the presence of cascades 734-192-191 keV and 790-192-192 keV are evident from the double gates shown in Figs. 6(a)–6(c). The above facts point towards the multiple placements of the 192 keV transition. From Figs. 6(a) and 6(b), it is clear that 734 and 790 keV select parallel cascades with two different transitions of the nearby energies of 517 and 519 keV, respectively. The set of transitions connected by 734 keV to the band B1 is identified as a separate band structure B2. Figure 6(c) shows that the 192-192 keV cascade is in coincidence with both the 734 and 790 keV transitions but not with either the 517 or 519 keV transitions. Thus the only possibility to place the second 191 (192) keV transition is in parallel with 517 (519) keV. The presence of the 326 and 327 keV transitions in coincidence with 734 and 790 keV, respectively, confirm the placement of the 326-191 keV and 327-192 keV cascades in parallel to 517 (band B2) and 519 keV (band B1) respectively, as shown in Fig. 4. The pure $E2$ nature of 734 and 790 keV are determined from their R_{DCO}

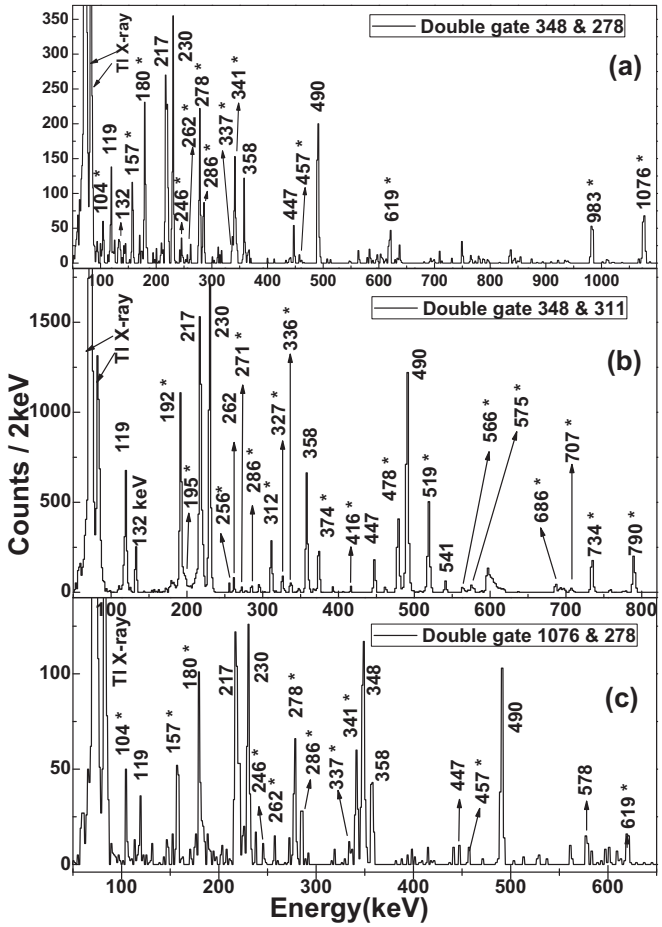

FIG. 5. Coincidence spectra corresponding to double gates of (a) 348 and 278 keV, (b) 348 and 311 keV, and (c) 1076 and 278 keV transitions pertaining to the bands B1 and B3 in ^{200}Tl. Transitions marked with "*" are newly placed in the level scheme.

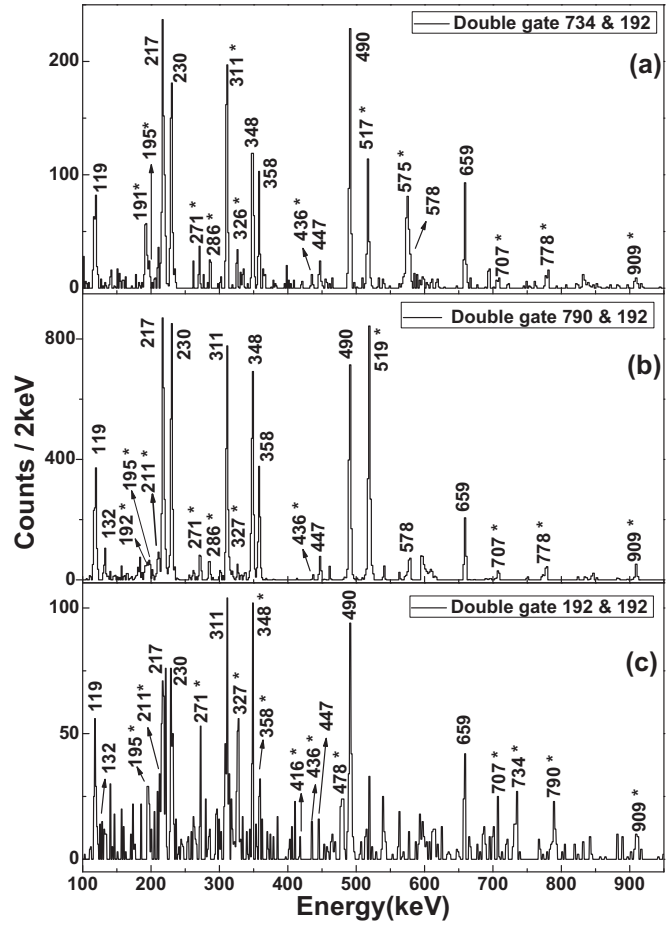

FIG. 6. Coincidence spectra corresponding to double gates of (a) 734 and 192 keV, (b) 790 and 192 keV, (c) 192 and 192 keV corresponding to the transitions of bands B1 and B2 in ^{200}Tl. Transitions marked with "*" are newly placed in level scheme.

and Δ_{IPDCO} measurements, as clearly seen from Fig. 2 and Table I. Thus, the R_{DCO} and Δ_{IPDCO} of 517 and 519 keV transitions were deduced from respective coincidence spectra of the 734 and 790 keV transitions. It was found that the 517 keV transition is of $M1$ character, whereas the nature of the 519 keV transition is $E2$. The observation of the 191 keV γ ray in the double gate of 734 and 192 keV supports the placement of a 57 keV transition between 3856.8 and 3799.5 keV levels. However, this low-energy transition could not be observed because of a low energy threshold at about 50 keV in the present experiment. The R_{DCO} and Δ_{IPDCO} of 192 keV, placed between the 4048.8 and 3856.8 keV levels could be found from the 519 keV gate, because only this particular 192 keV is in coincidence with 519 keV. The 192-327 keV cascade, in parallel to 519 keV, was found to be very weak and their multipolarities could not be deduced directly from R_{DCO} measurements and therefore were assumed to be of $(M1 + E2)$ character. The intensities of γ rays placed in the level scheme above the 4048.8 keV state of band B1 were relatively weak but their placements could be confirmed from the added double gates of strong transitions of band B1. All the spins and parities of the states in band B1 above the 3856.8 keV (18^-) level were deduced from the coincidence spectrum corresponding to the 519 keV gate, which was established as a stretched $E2$ transition. The spins and parities of band B2 have been confirmed from the 734 keV gate.

Few γ rays of 971, 997, and 1368 keV have been placed in the level scheme in parallel to each other, connecting to the 1659.3 and 1889.1 keV levels, respectively, of the band B1. The placement of these could be confirmed on the basis of the following coincidence conditions: The 971 keV γ ray was found to be in coincidence with 119 and 217 keV but not with 230 keV. The 997 and 1368 keV γ rays were found to be in coincidence with 119, 217, and 230 keV, but not with any other γ rays beyond the 1889.1 keV level of band B1.

The connection of band B1 to the 1244.0 keV level was confirmed from the fact that all the transitions of band B1 were found to be in coincidence with the 490 keV transition, decaying out from the 1244.0 keV level. This is evident from the coincidence spectrum of Fig. 1, obtained from γ-γ matrix and the double gates shown in Figs. 5 and 6, obtained from the γ-γ-γ cube. However, it was also confirmed that the 490 and 494 keV transitions are not in coincidence with each other. Therefore, the 1244.0 and 1247.4 keV levels must

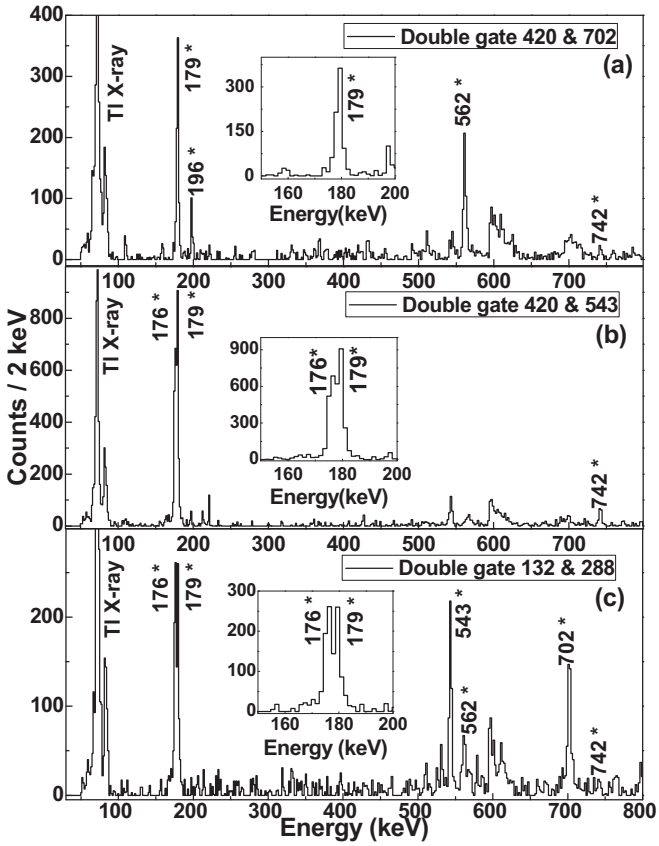

FIG. 7. Coincidence spectra corresponding to double gates of (a) 420 and 702 keV, (b) 420 and 543 keV, (c) 132 and 288 keV transitions corresponding to the band B4 in ^{200}Tl.

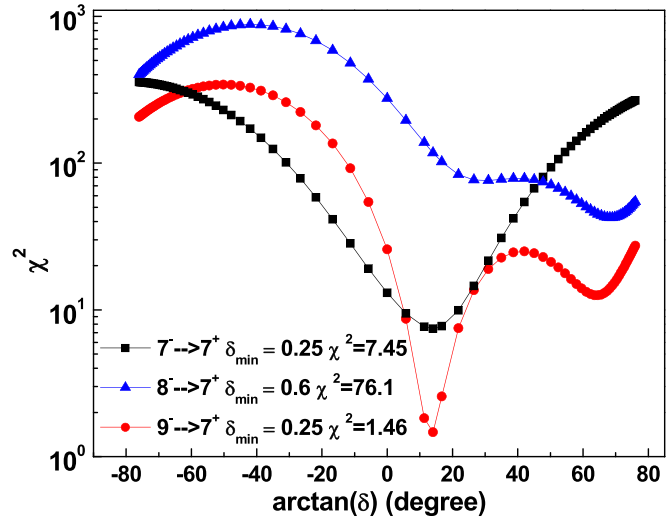

FIG. 8. $\chi^2(\delta)$ analysis of angular distribution and polarization of 490 keV transition.

be connected by an unobserved 3 keV transition, as also reported in Ref. [12]. In the present work, the spin-parity of the 1244.0 keV 4.8 ns isomeric level has been determined as 9^-, in contrast to the assignment of 7^- by Kreiner *et al.* [12]. The assignment of 9^- to the 1244.0 keV level was based on the DCO ratio and polarization measurements of the decaying 490 keV transition along with the detailed analysis of angular-distribution data. The DCO ratio of the 490 keV transition was obtained from the the 659 keV pure $E2$ gate, as the other dipole transitions below 659 keV in band B1 have mixing of higher multipolarities. The DCO ratio of 1.01(2) from the 659 keV gate results in a quadrupole character of the 490 keV transition. The 230 keV transition in the same cascade was found to be of predominantly of $M1$ character from its DCO ratio in 659 keV gate. So the DCO ratio of the 490 keV transition was also cross-checked from the gate of 230 keV and a value of 2.00(2) was obtained, supporting the quadrupole character of 490 keV. The measurement of Δ_{IPDCO} of the 490 keV transition clearly indicates the 490 keV transition to be of magnetic character. The values of the DCO ratio and Δ_{IPDCO} of 490 keV fall into the $M2$ region in Fig. 2. The quadrupole nature of 490 keV is also evident from the independent measurement of its angular distribution data, obtained in singles mode, as shown in Fig. 3(e). The conclusion about the nature of the 490 keV transition, which determines the spin-parity of the 1244.0 keV level, was obtained by comparing the above experimental data related to 490 keV with various calculations. The polarization (P) and angular distribution coefficients (a_2, a_4) were calculated [24] for the J_i^π to J_f^π cases of 7^- to 7^+, 8^- to 7^+, and 9^- to 7^+ for various mixing ratios δ. A $\chi^2(\delta)$ analysis [25] of the present data, considering both angular distribution and polarization measurements of the 490 keV transition, was then carried out and is shown in Fig. 8. It can be seen that the χ^2 values of 7.45, 76.12, and 1.46 are obtained for 7^- to 7^+, 8^- to 7^+, and 9^- to 7^+, respectively, resulting in a minimum χ^2 for the case of 9^- to 7^+ with lowest mixing ratio δ. A similar $\chi^2(\delta)$ analysis for the DCO ratio of 490 keV was also carried out by calculating the DCO ratio of 490 keV for three possible spin sequences of 7 to 7, 8 to 7, and 9 to 7 by using the code ANGCOR [26] and considering the multipolarity and spin sequence of all the intermediate transitions between 490 keV and the gating on the transition at 659 keV. It has been found that the spin sequence of 9 to 7 corresponds to the minimum χ^2 value for the DCO ratio of the 490 keV transition. With the above analysis, it was concluded that the 9^- to 7^+ assignment to the 490 keV transition is the most probable and therefore a spin-parity of 9^- was assigned to the 1244.0 keV level. The 9^- assignment to the 1244.0 keV level is also consistent with the Weisskopf estimate of the half-life of 32 ns for this level in comparison with the reported measured half-life of 4.8 ns. The 220 keV transition, decaying out from this 1244.0 keV level and the 262 keV transition, following the 220 keV transition, were found to be of $E2$ and $E1$ character, respectively, from the present measured values of R_{DCO} and Δ_{IPDCO}. Thus, the spin-parity assignment of the 762.0 and 1023.6 keV levels were also modified as 6^+ and 7^-, respectively, compared with previous work [12]. The multipolarity of the 221 keV transition between the 762.0 and 540.9 keV levels could not be determined in this work because of the 330 ns lifetime of the 762.0 keV level. However, the assignment of spin-parity of 6^+ to the 762.0 keV level fixes the nature of the 221 keV transition as $M2$ type. The Weisskopf estimate of a half-life

of 1.77 μs for this transition also corroborates well with the measured half-life of 0.33 μs of this 762.0 keV level. This fact is further consistent with the assignment of spin-parity of 9^- to the 1244.0 keV level.

The double gates shown in Fig. 5 establish the presence of a band B3, connected to the main yrast band B1 at the 2237.4 keV (13^-) level the by 983 and 1076 keV transitions. From Figs. 5(a) and 5(b) it can be clearly seen that all the transitions of band B3 are in coincidence with the 348 keV transition of band B1, but not with the other higher-spin members of the band B1 beyond the 2237.4 keV level. The connections of bands B3 and B1, i.e., the 983 and 1076 keV transitions, can be seen from Fig. 5(a) and all other coincident transitions of band B3 are evident from the double gate of 1076 and 278 keV, shown in Fig. 5(c). The double placement of 278 keV γ ray is also clear from this spectrum. The intensities of the 278 keV doublet were estimated by subtracting the intensity of the 278 keV transition in the gate of 619 keV from the total intensity with proper normalization. The relative placements and coincidence relationships of the observed transitions of band B3 are checked from gated spectra corresponding to various γ rays. The 1076 keV transition is found to be of $E1$ type from R_{DCO} and Δ_{IPDCO} measurements, as shown in Table I, which fixes the parity of the new band B3 as positive. The 983 keV transition is found to be of quadrupole character from the R_{DCO} measurements as well as from the angular distribution. The quadrupole nature of 983 keV along with its measured Δ_{IPDCO} make it a $M2$-type transition. The R_{DCO} and Δ_{IPDCO} ratios for the low-energy 93 keV transition cannot be found but its assignment is fixed by determining the spin-parity of the 3313.4 and 3220.3 keV levels.

The band (B4) is also extended up to an excitation energy of 2634.0 keV. The 132 and 288 keV transitions of this band and the 420 keV crossover transition, placed in parallel to the 132-288 keV cascade, were known from previous work [12]. In Ref. [12], a 176 keV γ ray was also placed above the 1173.7 keV level, but in the present work two γ rays with the nearby energies of 176 and 179 keV have been observed and placed in the level scheme from the intensity balance and coincidence relationships of the transitions in band B4. From Figs. 7(a) and 7(b), it is also evident that two parallel branches starting with the 543 and 702 keV transitions are present above the 1173.7 keV level. The 702 keV transition is in coincidence with only 179 keV, but the 543 keV transition is in coincidence with both 176 and 179 keV. The observation of 179 keV in the double gate of 420 and 702 keV [Fig. 7(a)], establishes the presence of a 16 keV unobserved transition from 1892.5 keV to 1876.0 keV level. The spin-parity of the 886.0 keV level of band B4 was fixed as 8^+ from the fact that 358 keV $E1$ transition decays to this level from the 1244.0 keV (9^-) level of band B1. The 132 keV transition between the 886.0 (8^+) and 753.6 (7+) keV states was found to be an ($M1 + E2$) transition from the DCO ratio analysis, although the Δ_{IPDCO} could not be determined for this low-energy transition, because it did not have significant scattering to the neighboring crystal of the clover detectors. The angular correlation was also calculated by using the code ANGCOR [26] which suggests a 132 keV transition to be of mixed multipolarity. For the 420 keV transition, as it is not in coincidence with any of the known pure transitions; its DCO ratio could not be determined. But the angular distribution of 420 keV transition suggests it to be of dipole nature and the Δ_{IPDCO} value indicates the mixed nature of this transition. Thus the spin-parity of the 1173.7 keV has been assigned as 8^+. Angular distribution of the 288 keV transition suggests it to be of quadrupole nature, but the spin of the 1173.7 keV transition makes it a nonstretched $M1 + E2$ (8^+ to 8^+) transition. The tentative spin-parity of the other levels in band B4 have been determined from the R_{DCO} values of the 702, 562, 543, and 176 keV transitions from the 132 keV gate. Although the 132 keV transition is found to be of mixed type, the R_{DCO} values of the 702, 562, 543, and 176 keV transitions in the 132 keV gate were compared with the theoretical angular-correlation calculation taking into account the mixing of the gating transition 132 keV. For none of the above transitions could Δ_{IPDCO} be obtained due to their weak intensities. Thus the spin-parity of band B4 above 1173.7 keV was assigned tentatively. The coincidence relationships among the various transitions of bands B4 and B1 establish 179 keV as the connecting transition between the 1892.5 keV (11^+) level of band B4 to the 2071.7 keV (12^-) level, which is in turn connected to the main band B1 by a 412 keV transition. This means 179 keV is of $E1$ character. The band B4 is also connected to the band B1 at 3337.8 keV level by 774 and 492 keV transitions in cascade. The presence of the 492 keV transition could be established from the double gate of 519 keV (of band B1) and 288 keV (of band B4). As the spin-parities of the 3337.8 keV and 2071.7 keV levels are fixed at 16^- and 12^-, respectively, the 492 and 774 keV transitions between these two levels are assigned as $E2$. This is also corroborated by the DCO ratio of these two transitions, as shown in Table I, although Δ_{IPDCO} could not be measured because of their weak intensities.

V. DISCUSSION

The proton and the neutron Fermi levels in ^{200}Tl lie just below the $Z = 82$ and $N = 126$ spherical shell closure, with one proton and seven neutrons removed from the closed shell. For the odd proton, the shell-model positive-parity $s_{1/2}$, $d_{3/2}$ and negative-parity $h_{9/2}$ orbitals are available and indeed the configuration of the ground and the first-excited states in the neighboring odd-A Tl isotopes are known to be $1/2^+$and $3/2^+$, respectively. For the odd-neutron hole, the negative-parity orbitals $p_{1/2}$, $p_{3/2}$, and $f_{5/2}$ are available to generate the low spins, whereas the unique positive-parity high-j $i_{13/2}$ orbital comes into play at higher spins. Thus, for the odd-odd ^{200}Tl, the low-spin states will have negative parity with configuration resulting from the above orbitals for odd-proton and odd-neutron holes [15]. The 2^- ground state and low-lying 3^- and 4^- states in ^{200}Tl are obtained from the $\pi s_{1/2} \otimes \nu f_{5/2}$ and $\pi d_{3/2} \otimes \nu f_{5/2}$ configurations. The 7^+ isomeric state observed in the odd-odd Tl isotopes has the dominant configuration of $\pi s_{1/2} \otimes \nu i_{13/2}$ coupled to a weakly deformed oblate core of ^{198}Hg. The low-lying 6^+ state at 762.0 keV is also likely to have the same configuration. In ^{198}Tl, this 6^+ state is known at similar excitation energy of 674 keV [11].

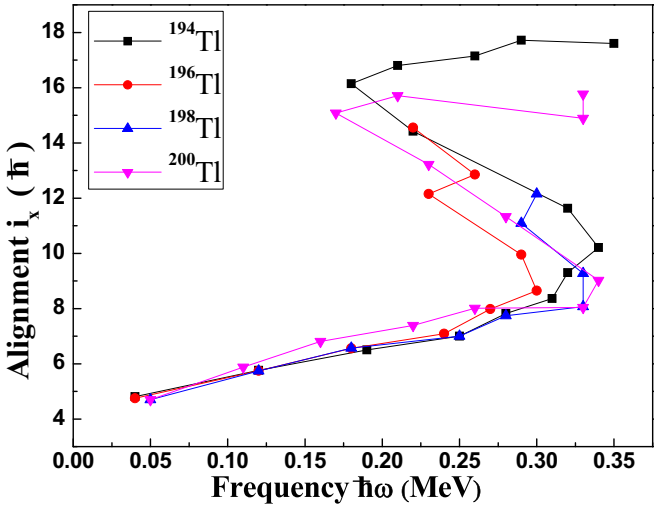

FIG. 9. Alignment plot for the $\pi h_{9/2} \otimes \nu i_{13/2}$ bands in odd-odd Tl isotopes. The level energies of the same bands of $^{194-198}$Tl are taken from Refs. [9,10,14], respectively. The Harris reference parameters are taken as $J_0 = 8\hbar^2$ MeV^{-1} and $J_1 = 40\hbar^4$ MeV^{-3}.

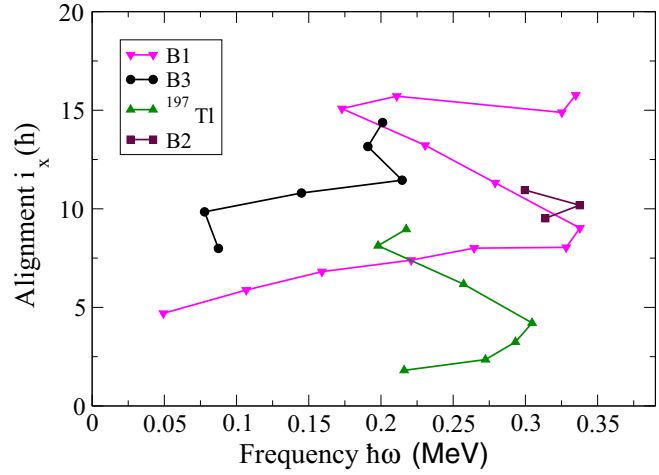

FIG. 10. Alignment i_x as a function of rotational frequency $\hbar\omega$ for the bands in ^{200}Tl. The same for the $9/2^-$ band in the odd-proton nucleus ^{197}Tl is also shown. The Harris reference parameters are taken as $J_0 = 8\hbar^2$ MeV^{-1} and $J_1 = 40\hbar^4$ MeV^{-3}.

A. Band B1

The deformation-driving intruder $h_{9/2}$ orbital becomes available for the odd proton in Tl isotopes for oblate deformation and band structure with collective features having intrinsic configuration of $\pi h_{9/2} \otimes \nu i_{13/2}$ have been identified in all odd-odd Tl isotopes in the $A = 190$–200 mass region. Isomeric states based on the $\pi h_{9/2}$ configuration in ^{199}Tl and on the $\nu i_{13/2}$ configuration in ^{199}Hg are known at the excitation energies of 748.9 and 532.5 keV, respectively, and oblate band structures have been identified for both the cases based on those configurations. In the case of ^{200}Tl, the excited state corresponding to the $0^+(^{198}\text{Hg}) \otimes \pi h_{9/2} \otimes \nu i_{13/2}$ configuration is, therefore, expected at an excitation energy of $(748.9 + 532.5 =)1281.4$ keV. The excitation energy of the 8^- bandhead of the observed band structure (B1) has been found to be at 1247.4 keV, which is in very good agreement with the expected energy of the above configuration. Therefore, the band B1 is identified to have the configuration $\pi h_{9/2} \otimes \nu i_{13/2}$.

To understand the collective features and band crossing in ^{200}Tl, the aligned angular momentum i_x has been plotted as a function of rotational frequency in Fig. 9 for the $\pi h_{9/2} \otimes \nu i_{13/2}$ bands in odd-odd thallium isotopes. This figure shows that the first band crossing for the $\pi h_{9/2} \otimes \nu i_{13/2}$ band (band B1) in ^{200}Tl occurs at a rotational frequency of $\hbar\omega = 0.34$ MeV. The gain in alignment after the first crossing is about $7\hbar$. The crossing frequency and gain in alignment in ^{200}Tl are very similar to those in the lighter odd-odd isotopes of thallium, as shown in Fig. 9. The band crossing in the lighter thallium isotopes are attributed to the alignment of a pair of neutrons in the $i_{13/2}$ orbital, which seems to be the case for ^{200}Tl as well. The similarities in the alignment gain and frequencies show that the collective rotational nature of the $\pi h_{9/2} \otimes \nu i_{13/2}$ band for the Tl isotopes still persists for ^{200}Tl, having similar deformation.

The alignment gain due to protons and neutrons in an odd-odd nucleus can be interpreted from the systematics of the neighboring odd-proton and odd-neutron nuclei. Unfortunately, the data on the two immediate odd-neutron and odd-proton neighbors, i.e., on ^{199}Hg and ^{199}Tl, respectively, are not enough for a good systematic comparison. But some inferences may be drawn from the alignment plot of ^{197}Tl, for which the data do exist up to above the band crossing. The alignment for ^{197}Tl along with those for different bands in ^{200}Tl are shown in Fig. 10. It can be seen that the initial alignment of band B1 in ^{200}Tl is about $5.5\hbar$ higher than the initial alignment in ^{197}Tl. The extra alignment is due to the odd neutron in ^{200}Tl which is in the $i_{13/2}$ orbital. The large difference indicates that the odd neutron must lie in the low-Ω orbital of $i_{13/2}$. From the Nilsson diagram one can see that it is true for oblate deformation because the $\nu 1/2^+[660]$ and $\nu 3/2^+[651]$ Nilsson orbitals are situated near the neutron Fermi level of ^{200}Tl at an oblate deformation of $\epsilon \sim 0.1$. In the present work, the band B1 has been extended to higher spins beyond the first band crossing, similar to recently observed high-spin structures in ^{194}Tl [13].

The energy staggering, defined by $S(I) = [E(I) - E(I-1)]/2I$, where $E(I)$ is the energy of the state with spin I, is plotted as a function of spin I for the band B1 in Fig. 11, along with the same bands in $^{194-198}$Tl. It can be seen from this figure that the staggering plots of all odd-odd Tl isotopes show remarkable similarity including the low-spin signature inversion at $11\hbar$. This signature inversion was interpreted [7] as due to the J dependence of the residual p-n interaction. The similarities in the staggering plot indicates no appreciable change in the residual p-n interaction in the Tl isotopes even for neutron numbers as large as $N = 119$. It can be seen that they start to behave differently after the neutron pair alignment. However, all of them, except ^{194}Tl, show a second inversion at the similar spin of about $19\hbar$. As the level scheme of ^{200}Tl has been extended further in this work, it can observed that this second inversion is recovered quickly and follows the trend as

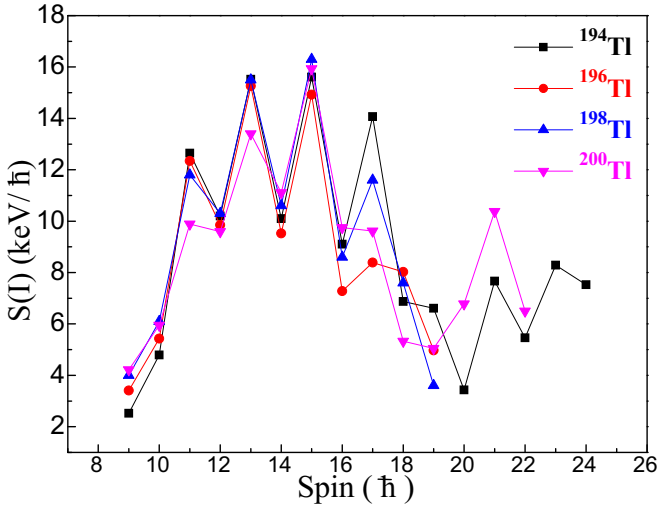

FIG. 11. Staggering $[S(I) = [E(I) - E(I-1)]/2I]$ plot for the $\pi h_{9/2} \otimes \nu i_{13/2}$ bands in odd-odd Tl isotopes. Data for $^{194-198}$Tl are taken from Refs. [9,10,14], respectively.

in the lighter isotope ^{194}Tl. It would be interesting to extend the level scheme of ^{196,198}Tl to see if they also behave similarly.

The assignment of two-quasiparticle (qp) configuration $\pi h_{9/2} \otimes \nu i_{13/2}$ to band B1 before band crossing and the four-quasiparticle configuration $\pi h_{9/2} \otimes \nu i_{13/2}^{-3}$ due to the alignment of a pair of neutrons in the $i_{13/2}$ orbital after the band crossing are also supported by the comparison of experimental $B(M1)/B(E2)$ values of band B1 with the theoretical ones. The theoretical $B(M1)$ and $B(E2)$ values were calculated by using the geometrical model following the prescription of Ref. [27]:

$$B(M1; I \to I-1) = \frac{3}{8\pi}[(g_p - g_R)A + (g_n + g_R)B]^2(\mu_N^2), \quad (4)$$

$$A = \left(1 - \frac{K^2}{I^2}\right)^{1/2} \Omega_p - i_p \frac{K}{I}, \quad (5)$$

$$B = \left(1 - \frac{K^2}{I^2}\right)^{1/2} \Omega_n - i_n \frac{K}{I}, \quad (6)$$

$$B(E2; I \to I-2) = \frac{5}{32\pi} {Q_0}^2 \cos^2(\gamma + 30^o)\left(1 - \frac{K}{I-1}\right)^2 (e^2b^2). \quad (7)$$

$g_{p(n)}$, $i_{p(n)}$, and $\Omega_{p(n)}$ in Eqs. (4)–(6) represent the g factor, alignment, and angular-momentum component on the symmetry axis for protons (neutrons). For the calculated $B(M1)/B(E2)$ in Fig. 12, the values for $K = 6$, $i_p = 1.5$, and $i_n = 6.5$ were taken from the band properties of neighboring odd-A nuclei. The values for g_p, g_n, and the rotational g factor were taken as 0.86, −0.16, and 0.3, respectively, from Ref. [7] and assumed to be same for the case of ^{200}Tl. An oblate shape with deformation $\beta_2 \sim 0.12$ has been assumed to calculate Q_0. Ω_p and Ω_n were taken as 4.5 and 1.5, respectively, corresponding to the occupation of the $\Omega = 9/2$ orbital for protons and the $\Omega = 3/2$ orbital for neutrons. The calculated and measured $B(M1)/B(E2)$ values are shown in Fig. 12. The good match of the experimental and calculated values before and after band crossing supports the assigned configurations of band B1. The experimental $B(M1)/B(E2)$ values are calculated by the formula

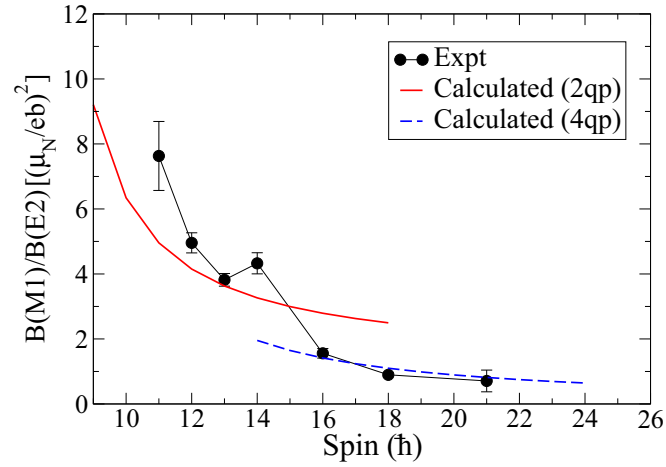

FIG. 12. Experimental $B(M1)/B(E2)$ of band B1 before and after band crossing is compared with that of calculation for two- and four-quasiparticle (qp) configurations (see text).

$$\frac{B(M1; I \to I-1; \gamma_1)}{B(E2; I \to I-2; \gamma_2)} = \frac{0.6968 E_{\gamma 2}^5}{\lambda E_{\gamma 1}^3 (1+\delta^2)} \left(\frac{\mu_N}{eb}\right)^2, \quad \lambda = \frac{I_{\gamma 2}}{I_{\gamma 1}}, \quad (8)$$

where $I_{\gamma 1}$ ($I_{\gamma 2}$) is the intensity of the transition γ_1 (γ_2) and δ is the mixing ratio of $M1$ with $E2$.

B. Band B2

The band B2 consists of a set of levels which lie very close to the levels in band B1 around the band-crossing region of band B1. The band diagram is shown in Fig. 13 for different bands in ^{200}Tl. It is evident from this plot that the band B2 lies very close to the main sequence of band B1. In fact, some of

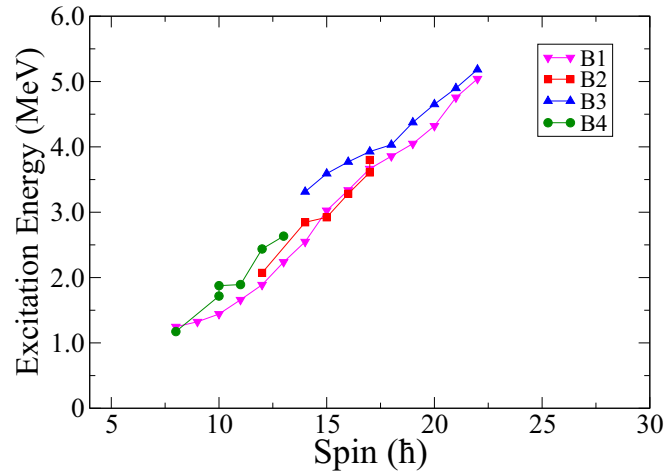

FIG. 13. Spin vs excitation energy plots of different bands in ^{200}Tl.

the levels in band B2 lie below those in band B1 for the same value of spin. Moreover, several interconnecting transitions have been observed between these bands. This indicates that the configurations of these two bands are similar, if not same.

It can be seen from Fig. 10 that the alignment values for band B2 are very similar to those for band B1 around the band-crossing region. Doubly degenerate bands for the $\pi h_{9/2} \otimes \nu i_{13/2}$ band have been reported in the neighboring odd-odd isotopes of ^{198}Tl and ^{194}Tl [13,14]. The side bands in those cases were observed in the lower-energy region before the band crossing. In ^{200}Tl, we have not observed any indication of such bands in the lower-energy region, but it is interesting to note the similarities in bands B1 and B2 around the band-crossing region. However, whether these bands can be considered as doubly degenerate bands are yet to be confirmed because the side bands are not well developed.

A possible alternate interpretation for band B2 can also be given in terms of the alignment of a pair of protons. The $\pi h_{11/2}$ alignment has been observed in the odd-A Hg isotopes ^{193,195}Hg [28,29] after the neutron pair alignment. However, as the neutron number increases, the neutron alignment frequency also increases and it may so happen that the proton and neutron alignment frequency becomes similar at ^{200}Tl. The cranked shell-model calculations (discussed in the next section) shows that the proton crossing is expected at a slightly higher rotational frequency of $\hbar\omega \sim 0.4$ MeV. As the $\pi h_{11/2}$ orbital is also a high-j orbital like $\nu i_{13/2}$ and similar to the neutrons, the proton alignments will also take place in the upper half of the $\pi h_{11/2}$ orbital for oblate deformation. Therefore, the alignment gain for the protons would be similar to those of neutrons, as observed.

C. Band B3

Band B3 has been assigned as a positive-parity band based on the 14^+ state at 3.3 MeV of excitation energy. The excitation energy of this band, as can be seen in Fig. 13, indicates that it should have a four-quasiparticle (qp) nature. This band has strong decay paths to band B1. Therefore, the configuration of this band is expected to have similarities with band B1. In comparison with the similar band observed in ^{198}Tl [30] and the available single-particle levels near the Fermi surface, the configuration of band B3 is assigned as $\pi h_{9/2} \otimes \nu i_{13/2}^{-2} \nu(f_{5/2}p_{3/2})$. It may be noted here that the spin and the excitation energy of the bandhead of this band in ^{198}Tl was observed at lower values. In the present work, we have not observed the lower-spin members of this band. The alignment plot in Fig. 10 shows that this band has about $4\hbar$ of additional alignment than the two-qp band B1 but has relatively less alignment compared with the four-qp part of band B1 that is after the alignment of a pair of neutrons in the $i_{13/2}$ orbital in band B1. It therefore suggests that, out of the two additional neutrons in this four-qp band, one should be in a low-j orbital and hence support the assigned configuration.

D. Band B4

The sequence B4 does not represent a well-formed rotational band. It can be seen from Fig. 13 that this band remains within the two-qp part of the main band. The 8^+ state in ^{200}Tl can be obtained from the coupling of $\pi d_{3/2}$ and $\nu i_{13/2}$ with the ground state in ^{198}Hg. The $\pi d_{3/2}$ state in ^{199}Tl is situated at 367 keV excitation energy and the $\nu i_{13/2}$ state in ^{199}Hg at 532 keV. The 886.0 keV excitation energy of the 8^+ state in ^{200}Tl is in excellent agreement with the sum of these two excitation energies. Moreover, the $5/2^+$ state corresponding to the $\pi d_{5/2}$ orbital in ^{199}Tl is situated about 350 keV above its $\pi d_{3/2}$ state. The excitation energy of the second 8^+ state in ^{200}Tl is close to this. Therefore, the possible configuration of the two 8^+ states in ^{200}Tl is $\pi(d_{3/2},d_{5/2}) \otimes \nu i_{13/2}$.

E. Other states and structures

A sequence of levels starting with the 7^- state at 1023.6 keV has been observed up to the 9^- state. Assuming a rotational structure, an aligned angular momentum of about $3\hbar$ has been obtained for this structure. The most probable configuration for this structure would be $\pi h_{9/2} \otimes \nu i_{13/2}$ but involving the $\Omega = 9/2$ and $5/2$ orbitals in protons and neutrons, respectively. The configuration of the 12^- state at about 2071.7 keV in ^{200}Tl can be assigned from the coupling of the low-lying states in ^{200}Tl with the two-neutron state in ^{198}Hg [31]. The first negative-parity bandhead in ^{198}Hg is a 5^- state at 1.6 MeV of excitation energy with a configuration of $\nu i_{13/2}\nu p_{3/2}$. We assign the configuration of the 12^- state at 2071.7 keV in ^{200}Tl as the coupling of its 7^+ state ($\pi s_{1/2} \otimes \nu i_{13/2}$) with the 5^- state in ^{198}Hg. This state can also be formed from the two maximally aligned quasiparticles in $\pi h_{11/2}$ and $\nu i_{13/2}$ orbitals. It was predicted to be at about 1.7 MeV in the neighboring isotope ^{198}Tl [10] for a deformation of $\beta_2 \sim 0.15$. A tentatively 12^- state observed in the same nucleus at an excitation energy of 1736.0 keV might correspond to this state [30]. However, no well-developed rotational band structure is observed on top of this band in either of the nuclei, although the similar configuration yielded very-well-developed band structures in $^{190-194}$Au nuclei [32].

VI. TOTAL ROUTHIAN SURFACE CALCULATIONS

To have information on the deformation of the band structures in ^{200}Tl, total Routhian surface (TRS) calculations were performed by the Strutinsky shell correction method using a deformed Woods–Saxon potential for the calculation of the single-particle shell energies with Lipkin–Nogami pairing [33–36]. The universal parameter set was used for these calculations [37]. The Routhian energies were calculated in (β_2,γ,β_4) deformation mesh points with minimization on β_4. The procedure of such calculations have been outlined in Ref. [38]. The Routhian surfaces are plotted in the conventional β_2-γ plane.

The TRS plot for the bandhead of $\pi h_{9/2} \otimes \nu i_{13/2}$ band in ^{200}Tl is shown in Fig. 14 for the rotational frequency of $\hbar\omega = 0.0$ MeV. It can be seen that a minimum occurs at an oblate deformation ($\gamma = -60^\circ$), similar to those calculated for the neighboring isotopes ^{194,198}Tl for the same configuration [9]. However, the value of deformation $\beta_2 = 0.13$ obtained in ^{200}Tl is slightly less compared with the lighter isotopes for which $\beta_2 \sim 0.15$ was obtained. The similarities in the calculated

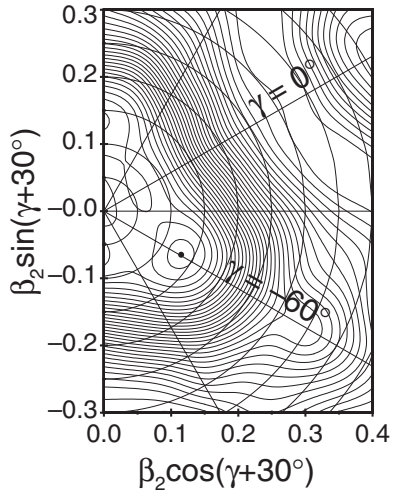

FIG. 14. Total Routhian surface (TRS) calculations for the band B1 with configuration of $\pi h_{9/2} \otimes \nu i_{13/2}$ in ^{200}Tl for rotational frequency $\hbar\omega = 0.0$ MeV. $\gamma = 0°$ and $\gamma = -60°$ lines correspond to prolate and oblate deformations, respectively. The contours are in 400 keV intervals.

deformations for the odd-odd Tl isotopes corroborate well with the similarities in their alignment and staggering plots. The calculations also show that the nice minimum observed at oblate deformation continues up to the rotational frequency of $\hbar\omega = 0.30$ MeV. At higher frequencies, the minima disappear and the surfaces become γ soft with larger deformation β_2. This γ softness continues even at higher rotational frequencies of $\hbar\omega = 0.50$ MeV for this configuration. It may be noted that the experimental band crossing is observed at a rotational frequency of $\hbar\omega = 0.34$ MeV in this band. A typical TRS plot at higher rotational frequency for this configuration is shown in Fig. 15, corresponding to a rotational frequency of $\hbar\omega = 0.45$ MeV. It indicates that the nucleus ^{200}Tl becomes γ soft after the band crossing.

For the 7^- ($\pi 9/2^-[505] \otimes \nu 5/2^+[642]$) state we have performed configuration-constrained potential-energy-surface

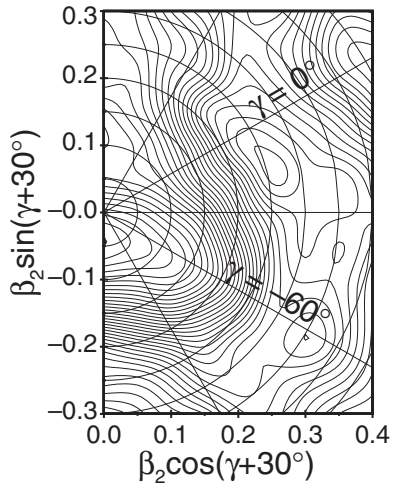

FIG. 15. Same as Fig. 14 but for $\hbar\omega = 0.45$ MeV.

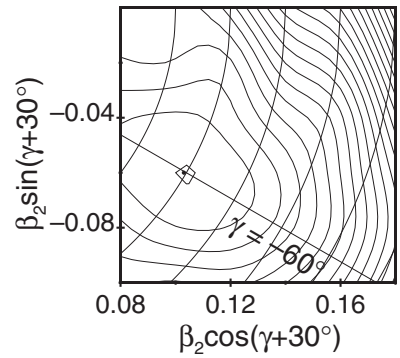

FIG. 16. Calculated configuration-constrained potential-energy surface for the 7^- state with the configuration of $\pi 9/2^-[505] \otimes \nu 5/2^+[642]$ in ^{200}Tl. The contours are in 400 keV intervals.

calculations in which the given orbits are tracked and blocked by using the average Nilsson number technique [39] and are shown in Fig. 16. The minimum in this case occurs almost at the same deformation as in band B1 at $\beta_2 = 0.12$ and $\gamma = -60°$. However, the energy at the minimum is somewhat higher than the minimum obtained for band B1. The difference increases with rotational frequency and the higher spin states in the 7^- band quickly become nonyrast. This is the possible reason for not observing this 7^- band to develop up to higher spins.

The TRS plot for the four-qp configuration of $\pi h_{9/2} \otimes \nu i^{-2}_{13/2} \nu(f_{5/2} p_{3/2})$ corresponding to band B3 is shown in Fig. 17. This plot shows that a minimum occurs at a triaxial deformation of $\gamma \sim 40°$ with $\beta_2 \sim 0.14$. A second minimum, within an energy gap of about 500 keV is also seen along the oblate ($\gamma \sim -60°$) axis with a slightly smaller deformation of $\beta_2 \sim 0.12$.

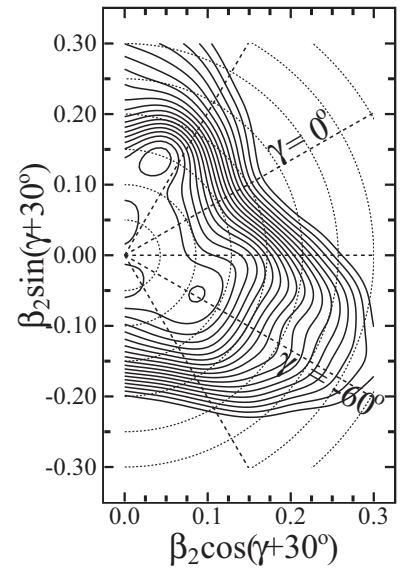

FIG. 17. Same as Fig. 14 but for the $\pi h_{9/2} \otimes \nu i^{-2}_{13/2}(f_{5/2} p_{3/2})$ four-qp configuration corresponding to the band B3 in ^{200}Tl at the rotational frequency $\hbar\omega = 0.11$ MeV. The contours are 400 keV apart.

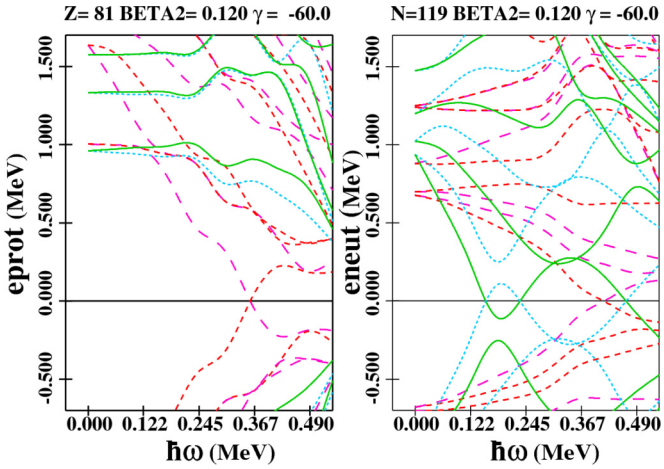

FIG. 18. Plots of single-proton (left) and single-neutron (right) Routhians of ^{200}Tl as a function of rotational frequency $\hbar\omega$ for deformation parameter $\beta_2 = 0.12$ and $\gamma = -60^\circ$ (corresponding to the calculated deformation of band B1). Solid (green) and dotted (cyan) lines correspond $\alpha = +1/2$ and $\alpha = -1/2$ signature partners, respectively, for the positive-parity orbitals while large-dashed (pink) and dashed (red) lines correspond to the same signature partners for the negative-parity orbitals.

The single-particle Routhians calculated for protons and neutrons in ^{200}Tl are also calculated and plotted as a function of rotational frequency $\hbar\omega$ in Figs. 18 and 19 for two deformation parameters corresponding to bands B1 and B3, respectively. It can be seen from Fig. 18 that the second neutron crossing of the positive-parity orbital (originating from the $\nu i_{13/2}$ orbital) takes place at a rotational frequency of about $\hbar\omega = 0.35$ MeV, which is responsible for the observed band crossing in band B1. The calculated crossing frequency is in very good agreement with the observed band-crossing frequency of band B1 (see Fig. 10). The slope of a Routhian in Figs. 18 and 19 gives the aligned angular momentum corresponding to that orbital and, subsequently, the gain in alignment if band crossing corresponds to the particle alignment in that orbital. The slope of the neutron Routhians in Fig. 18, which correspond to the alignment of band B1, gives the alignment gain of $6.6\hbar$ which is in excellent agreement with the observed gain in alignment of band B1.

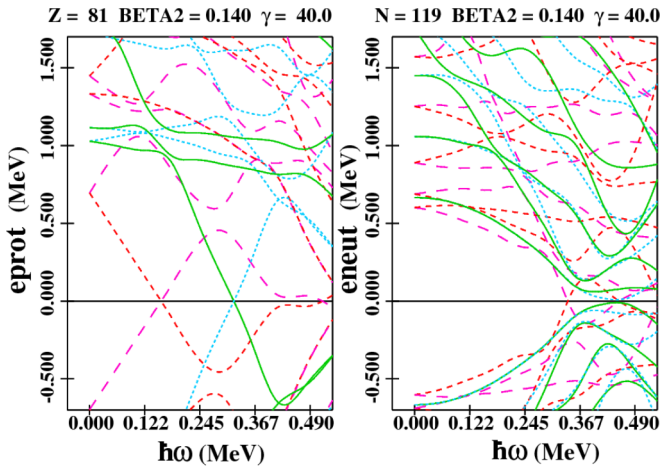

FIG. 19. Same as Fig. 18 but for deformation parameter $\beta_2 = 0.14$ and $\gamma = 40^\circ$ corresponding to the calculated deformation of band B3.

The single-proton Routhians in Fig. 18 show that the proton crossing takes place at a rotational frequency of about $\hbar\omega \sim 0.4$ MeV, which is slightly higher compared with the neutron-crossing frequency and also compared with the observed crossing frequency. However, the slope of the Routhians for the protons and the neutrons are very similar, as has been observed for bands B1 and B2. Band B2 might correspond to the proton pair alignment.

The calculated single-particle Routhians for protons and neutrons corresponding to the deformation of band B3 in ^{200}Tl are shown in Fig. 19. For this deformation, the proton crossing takes place at rotational frequency of $\hbar\omega \sim 0.26$ MeV, whereas the neutron crossing takes place at much higher frequency. The proton-crossing frequency is in good agreement with the observed crossing frequency of $\hbar\omega \sim 0.22$ MeV for the band B3. Therefore, it is suggested that the band crossing in this band is due to the alignment of a pair of protons in a negative-parity orbital. The slope of this Routhian gives an alignment gain of about $4\hbar$ and the observed gain in alignment seems to approach this value, as shown in Fig. 10.

VII. SUMMARY

High-spin states in ^{200}Tl have been populated by using the fusion evaporation reaction ^{198}Pt(^{7}Li ,$5n$) at the beam energy of 45 MeV and studied by γ-ray coincidence spectroscopic techniques using the INGA setup of 15 clover HPGe detectors. The level scheme of ^{200}Tl has been extended considerably up to the excitation energy of ~5.2 MeV and a spin of $22\hbar$ through the observation and placement of 60 new transitions in the level scheme. The spin and parity assignments were done by DCO, IPDCO, and angular distribution measurements. A few band structures involving the intruder $\pi h_{9/2}$ and high-j neutron orbitals have been observed in this odd-odd nucleus. The band structures are compared with the band structures in the other odd-odd Tl isotopes. It has been observed that the remarkable similarity in the $\pi h_{9/2} \otimes \nu i_{13/2}$ band in the odd-odd Tl nuclei continues to persists in the $N = 119$ isotope. The shape and band-crossing phenomena are discussed in the light of the cranking-model calculations with a Woods–Saxon potential. Oblate deformation is obtained for the two-qp bands in ^{200}Tl while the four-qp band seems to have a triaxial deformation. The band-crossing frequencies and the alignment gains in these bands are well reproduced by the cranking calculations. The calculations also predict that the $\pi h_{9/2} \otimes \nu i_{13/2}$ band becomes γ soft after the band crossing due to the alignment of a pair of neutrons in the $\nu i_{13/2}$ orbital. It would be interesting to extend the four-qp bands to higher rotational frequencies to compare their shape and alignment gains.

ACKNOWLEDGMENTS

The authors gratefully acknowledge the financial support by the Department of Science and Technology (DST), Government of India for the INGA project (Grant

No. IR/S2/PF-03/2003-II). The authors would like to thank all members of the INGA collaboration for setting up of the Clover HPGe Array at TIFR, Mumbai. The untiring efforts of the staff of the BARC-TIFR Pelletron LINAC facility at Mumbai are gratefully acknowledged for a providing good-quality beam. Special thanks are due to Professor R.G. Pillay for his guidance, encouragement, and stimulating discussion during the experiment. We acknowledge P.V. Isacker for a critical reading of the manuscript and useful comments. T.R., Md.A.A., and R.B. acknowledge with thanks the financial support received as research fellows from the Department of Atomic Energy (DAE), Government of India.

[1] I. Hamamoto, Phys. Rep. **10**, 63 (1974).
[2] K. Heyde *et al.*, Phys. Rep. **102**, 291 (1983).
[3] M. Huyse *et al.*, Phys. Lett. B **201**, 293 (1988).
[4] N. Fotiades, R. O. Nelson, M. Devlin, and J. A. Becker, Phys. Rev. C **76**, 014302 (2007).
[5] O. Hausser *et al.*, Phys. Lett. B **64**, 273 (1976).
[6] R. Broda *et al.*, Phys. Rev. C **84**, 014330 (2011).
[7] C. Y. Xie *et al.*, Phys. Rev. C **72**, 044302 (2005).
[8] A. J. Kreiner *et al.*, Phys. Rev. C **21**, 933 (1980).
[9] H. Pai *et al.*, Phys. Rev. C **85**, 064313 (2012).
[10] A. J. Kreiner, M. Fenzl, and W. Kutschera, Nucl. Phys. A **308**, 147 (1978).
[11] A. J. Kreiner, M. Fenzl, S. Lunardi, and M. A. J. Mariscotti, Nucl. Phys. A **282**, 243 (1977).
[12] A. J. Kreiner *et al.*, Phys. Rev. C **23**, 748 (1981).
[13] P. L. Masiteng *et al.*, Phys. Lett. B **719**, 83 (2013).
[14] E. A. Lawrie *et al.*, Phys. Rev. C **78**, 021305(R) (2008).
[15] R. E. Doebler, Wm. C. McHarris, and W. H. Kelly, Phys. Rev. C **2**, 2422 (1970).
[16] R. Palit *et al.*, Nucl. Instrum. Methods Phys. Res., Sect. A **680**, 90 (2012).
[17] D. C. Radford, Nucl. Instrum. Methods Phys. Res., Sect. A **361**, 297 (1995).
[18] R. K. Bhowmik, S. Muralithar, and R. P. Singh, Nucl. Phys. B **44**, 422 (2001).
[19] A. Srivastava *et al.*, Phys. Lett. B **718**, 931 (2013).
[20] A. Kramer-Flecken *et al.*, Nucl. Instrum. Methods Phys. Res., Sect. A **275**, 333 (1989).
[21] K. Starosta *et al.*, Nucl. Instrum. Methods Phys. Res., Sect. A **423**, 16 (1999).
[22] Ch. Droste *et al.*, Nucl. Instrum. Methods Phys. Res., Sect. A **378**, 518 (1996).
[23] S. Das Gupta *et al.*, Phys. Rev. C **88**, 044328 (2013).
[24] J. K. Deng *et al.*, Nucl. Instrum. Methods Phys. Res., Sect. A **317**, 242 (1992).
[25] L. P. Ekström and A. Nordlund, Nucl. Instrum. Methods Phys. Res., Sect. A **313**, 421 (1992).
[26] E. S. Macias *et al.*, Comput. Phys. Commun. **11**, 75 (1976).
[27] F. Dönau, Nucl. Phys. A **471**, 469 (1987).
[28] H. Hubel *et al.*, Nucl. Phys. A **453**, 316 (1986).
[29] N. Nenoff *et al.*, Nucl. Phys. A **629**, 621 (1998).
[30] E. A. Lawrie *et al.*, Eur. Phys. J. A **45**, 39 (2010).
[31] C. Günther *et al.*, Phys. Rev. C **15**, 1298 (1977).
[32] A. Neskakis *et al.*, Nucl. Phys. A **390**, 53 (1982).
[33] W. Nazarewicz *et al.*, Nucl. Phys. A **435**, 397 (1985).
[34] W. Nazarewicz *et al.*, Nucl. Phys. A **512**, 61 (1990).
[35] W. Satuła, R. Wyss, and P. Magierski, Nucl. Phys. A **578**, 45 (1994).
[36] F. R. Xu, W. Satuła, and R. Wyss, Nucl. Phys. A **669**, 119 (2000).
[37] J. Dudek, Z. Szymanski, and T. Werner, Phys. Rev. C **23**, 920 (1981).
[38] G. Mukherjee *et al.*, Nucl. Phys. A **829**, 137 (2009).
[39] F. R. Xu, P. M. Walker, J. A. Sheikh, and R. Wyss, Phys. Lett. B **435**, 257 (1998).